Supporting Information

A completely precious-metal-free alkaline fuel cell with enhanced performance using a carbon-coated nickel anode

Yunfei Gao,[a,1,2] Yao Yang,[b,1,3] Roberto Schimmenti,[c,4] Ellen Murray,[c] Hanqing Peng,[a] Yingming Wang,[a] Chuangxin Ge,[a,f] Wenyong Jiang,[a] Gongwei Wang,[a] Francis J. DiSalvo,[b] David A. Muller,[d,e] Manos Mavrikakis,[c] Li Xiao,[a,5] Héctor D. Abruña[b,5], Lin Zhuang[a,f,5]

[a]College of Chemistry and Molecular Sciences, Hubei Key Lab of Electrochemical Power Sources, Wuhan University, Wuhan 430072, China

[b]Department of Chemistry and Chemical Biology, Cornell University, Ithaca, NY 14853, USA

[c]Department of Chemical & Biological Engineering, University of Wisconsin-Madison, Madison, WI 53706, USA

[d]School of Applied and Engineering Physics, Cornell University, Ithaca, NY 14853, USA

[e]Kavli Institute at Cornell for Nanoscale Science, Cornell University, Ithaca, NY 14853, USA

[f]The Institute for Advanced Studies, Wuhan University, Wuhan 430072, China

[1]Y.G. and Y.Y. contributed equally to this work.

[2]Present address: Graduate School of Human and Environmental Studies, Kyoto University, Sakyo, Kyoto 606-8501, Japan.

[3]Present address: Miller Institute, Department of Chemistry, UC Berkeley, Berkeley 94720, USA.

[4]Present address: Center for Catalysis Theory, Department of Physics, Technical University of Denmark, Lyngby 2800, Denmark.

[5]To whom correspondence may be addressed. Email: hda1@cornell.edu; lzhuang@whu.edu.cn; chem.lily@whu.edu.cn

Table of Contents:

I. Detailed experimental descriptions

Material synthesis. Ni@CN_x were prepared by a facile method using purified nickel acetate and urea as the precursors. A typical synthesis method of Ni@CN_x included: 300 mg purified nickel acetate were mixed with 10, 20, 30 mg urea, respectively and then heated at 480 ºC in argon for 90 min. After fully cooling to room temperature, the product was ground in an agate mortar for 20 minutes. The mass ratio of urea to nickel acetate ($Ni(Ac)_2$) was controlled to be 1:30, 1:15 and 1:10, labeled as Ni@CN_x-1, Ni@CN_x-2 and Ni@CN_x-3, respectively.

Spinel oxides, $MnCo_2O_4$/C for the cathode electrode were synthesized using facile hydrothermal method[1]. $Co(Ac)_2 \cdot 4H_2O$ was dissolved in 15 mL deionized (DI) water and sonicated for 15 min. 500 µL of concentrated $NH_3 \cdot H_2O$ were diluted in 5 mL of DI water and added to the metal precursor solution dropwise under vigorous stirring at 1200 rpm. The pH of the formed metal-NH_3 complex solution was tested to be around 11. $Mn(Ac)_2 \cdot 4H_2O$ was subsequently added into the $[Co(NH_3)_6^{2+}]$ solution to maintain the cubic spinel structure. Ethanol (20 mL) was later added to the metal-NH_3 complex solution with an EtOH/H_2O volume ratio of 1:1. High surface-area carbon Ketjen Black (HSC KB) was added to achieve target metal oxide loadings of 80 wt.% in the catalyst/carbon composites. HSC KB was added to the suspension solution and stirred at 1200 rpm and 60 ºC for a 12 h ageing process. The solution was then transferred into a 50 mL autoclave for hydrothermal reaction at 150 ºC with an inner pressure of 30 bar for 3h. $MnCo_2O_4$ NPs supported on carbon were separated from the residual solution using a centrifuge at 6000 rpm and washed with EtOH/H_2O (vol. 1:1) three times and dried in oven at 80 ºC for 6h.

Material characterizations. Scanning transmission electron microscopy (STEM) images and elemental electron energy loss spectroscopy (EELS) maps were acquired on a fifth-order aberration-corrected STEM (Cornell Nion UltraSTEM) operated at 100 keV with a beam convergence semi-angle of 30 mrad. Sub-Ångström spatial resolution is achievable under such operating conditions. STEM images were processed using Richard-Lucy deconvolution (3 iterations). EELS spectral images were acquired with a 0.25 eV/channel energy dispersion (energy resolution, 1.0 eV) in a Gatan spectrometer with a size of 100~200 pixels and an

acquisition time of 10-20 ms/pixel. The Ni and C elemental maps were extracted using their sharp edges from EELS spectrum images and processed using principal component analysis (PCA, 3 components) and the linear combination of power law (LCPL) to subtract the background, in ImageJ software. The N signal was below the EELS detection limit due to the low N contents. Fine EELS spectra of Ni L edges with an energy resolution down to 0.5 eV were used to investigate the electron-loss near-edge structure (ELNES). Beam damage was routinely examined before and after the acquisition of EELS spectrum images (200×200 pixels, 10 ms/pixel). ELNES spectra were aligned by calibrating the high-loss (core-loss) spectrum against the low-loss (zero loss peak, ZLP) spectrum pixel by pixel (acquisition time: 10 ms/pixel) in dual EELS mode. Spectra alignment were performed using customized MATLAB code and ZLP was routinely examined to be precisely at 0.0 ± 0.1 eV to ensure the accuracy of the peak position for Ni L edges. The X-ray diffraction (XRD) patterns were recorded on a Rigaku Mini-flex 500 W diffractometer operated at 40 kV, 15 mA for Cu Kα (λ= 1.5406 Å) with a scanning speed of 10˚min^{-1}. The X-ray photoelectron spectroscopy (XPS) measurements were performed in a Thermo Fisher Scientific ESCALAB 250Xi XPS system with a monochromatic Al Kα X-radiation source. The Raman spectra were carried out in a Renishaw RM1000 with a scanning speed of 10 cm^{-1} s^{-1}. Transmission electron microscopy (TEM) images were recorded on a TECNAI G2 at 200kV. Samples were dispersed in ethanol and carried onto a copper support grid. The temperature-programmed desorption (TPD) was carried out in BELCAT-B CAT-201. Both of the samples were baked in air under 60 ºC before the test. The catalysts were first maintained in Ar (50mL/min) at 30 ºC for 30 min and heated in Ar from 30 ºC to 600 ºC with a ramping rate of 5 ºC/min using a thermal conducting detector (TCD).

Electrochemical measurements. Electrochemical tests were conducted on a CHI-634E potentiostat with a rotating disk electrode (RDE) system (Pine Research Instruments) at 25 ºC. The counter electrode was a sheet of carbon paper (Toray) and the reference electrode was a reversible hydrogen electrode (RHE) in 0.1 M KOH solution. When preparing a working electrode, a 10 mg catalyst sample was dispersed ultrasonically in 1ml diluted Nafion alcohol solution (0.05 wt%) to form an ink, and the ink was pipetted onto the RDE with a glassy carbon

(GC) substrate (Ø = 5 mm). The sample was then dried under an infrared lamp, and the resulting sample loading was 0.5 mg/cm^2. Both the cyclic voltammetry (CV) and hydrogen oxidation reaction (HOR) evaluation was in 0.1 M KOH solution at a sweep rate of 5mV/s. CV experiments were carried out in an Ar-saturated environment and HOR polarization profiles were measured in an H_2-saturated environment at a rotation rate at 2500 rpm. The accelerated durability tests (ADTs) were carried out in 0.1 M KOH solution by scanning the potential from -0.1 V to 0.5 V (vs. RHE) at 100 mV/s for 10,000 cycles.

Fuel cell tests. The fabrication of membrane-electrode assemblies (MEAs) and fuel cell tests were as same as previously reported.[2] Specifically, the catalyst ink was prepared with catalysts and QAPPT (Cl^- as anion) ionomer solution in n-propanol. Using QAPPT (Cl^- as anion) as membrane (15±5 μm in thickness) to fabricate the catalyst coated membrane (CCM), each side of the QAPPT membrane was sprayed with the ink. The area of the electrodes was 4 cm^2. The catalyst loadings for Pt/C in the cathode were 0.4 mg_{metal}/cm^2. Various Ni@CN_x loadings in the anode from 5 to 15 mg/cm^2, were tested to optimize the MEA performance. The CCM was subsequently immersed in 1.0 M KOH solution for 15 h to exchange the Cl^- anion to OH^-. Finally, the CCM was rinsed with deionized water for several times until the pH of the washing water was neutral.

Fuel cells were tested using a 850e Multi Range (Scribner Associates Co.) using humidified H_2 and O_2 gases. The cell temperature was set at 80 ºC, and the flow rate of both H_2 and O_2 gases was 500 mL/min with 0.2 MPa of backpressure. To obtain performance in H_2 mixed with 100 ppm CO, the reactant gas in the anode was shifted to a cylinder which contained pure H_2 and 100 ppm CO.

Computational Methods. We performed periodic density functional theory (DFT) calculations as implemented in the Vienna *Ab Initio* Simulation Package (VASP).[3,4] The core electron interactions were described using projector augmented wave (PAW) potentials. A plane wave basis set with a kinetic energy cutoff of 400 eV was used to expand the electronic wave function of the valence electrons. We used the generalized gradient approximation (GGA)

as implemented in the Perdew, Burke, and Ernzerhof (PBE)[5] exchange-correlation functional. Dispersion interactions were accounted for with Grimme-D2 semiempirical dispersion corrections.[6] PBE-D2 offers a good compromise between computational cost and accuracy for the description of van der Waals interactions in metal-graphene heterostructures.[7-9] All calculations were spin-polarized, allowing the systems to relax to their most stable spin state, giving Ni an average magnetic moment of 0.65 μ_B per atom, when free of adsorbates. Geometry optimizations were performed until the Hellman−Feynman forces on each atom were less than 0.02 eV $Å^{-1}$.

With these settings, the optimized Ni bulk lattice constant was determined to be 3.479 Å, in good agreement with the experimental value of 3.524 Å[10]. (15×15×15) and (6×6×1) Monkhorst–Pack[11] *k*–point meshes were used for bulk and surface calculations, respectively. A (10×10×1) *k*–point mesh was used for density of states (DOS) calculations. A Ni(111) extended model surface, periodically repeated in a 3×3 supercell comprising 4 layers, was used to model the Ni electrocatalyst surface. For all surface models, the bottom two layers of each supercell were kept fixed at the bulk lattice positions of Ni atoms. The remaining Ni layers and all adsorbates were allowed to fully relax. For surface calculations, we included at least 15 Å of vacuum between slabs in the z-direction and dipole corrections to avoid interactions between periodic unit cells.

To model the graphene coating of Ni (Ni@Graphene), we used a graphene model periodically repeated in a $3\sqrt{2}\times3\sqrt{2}$ supercell. The optimized geometry of Ni@Graphene is presented in Figure S21.

The XPS characterization of Ni@CN_x (see Figure S10) suggests that N defects are not in direct contact with the Ni surface. Thus, for models with N-defective coatings, we used 2 layers of stacked, graphene nanosheets where the N-defects were introduced only in the top graphene layer. The effect of N-defectivity was studied in the context of pyridinic (PYR) and pyrrolic (PYL) defects. The former constitutes the majority phase of defects according to XPS characterization. We studied two different PYR defect topologies. In the first case, PYR (3N), a C monovacancy is introduced and the three unsaturated carbon atoms are substituted by N

atoms. In the second pyridinic defect topology, PYR (4N), a C divacancy is introduced and the four unsaturated carbon atoms are substituted by N atoms. PYL defects are obtained by removing one carbon atom from the graphene sheet and substituting one unsaturated carbon with a N atom to form a pyrrolic ring. The energy-optimized geometry of Ni@CN_x models is presented in Figure S21. We note that PYL reconstructs to a reconstructed monovacancy geometry (PYL-r), previously experimentally determined through AC-TEM for pure graphene.[12] The same reconstruction is not encountered when a single Ni adatom is supported on the PYL defect (see Figure S26).

The binding energies (BE) of key HOR reaction intermediates and catalyst poisons (H*, OH*, and O*) on the Ni(111), Ni@Graphene and Ni@CN_x electrocatalyst models were calculated using the following expression:

$$BE = E_{tot} - E_{slab} - E_{gas}$$

where E_{tot} is the electronic energy of the system with H*, OH*, or O* adsorbed to a slab model, E_{slab} is the energy of the slab model without an adsorbate, and E_{gas} is the gas-phase energy of H, OH, or O, respectively.

To elucidate the relative stability of different defects, we calculated the defect formation energy (ΔE_{Def}) of each defect topology according to the following expression:

$$\Delta E_{def} = (E_{\mathrm{Ni@CNx}} - E_{\mathrm{Ni@Graphene}}) - \Delta X_N E_N - \Delta Y_C E_C$$

where $E_{Ni@CNx}$ is the total energy of Ni@CN_x model (including a PYR or PYL defect), ΔX_N and ΔY_C are, respectively, the difference between the number of N and C atoms present in Ni@CH_xH_y and Ni@Graphene. E_N is the electronic energy of a N atom calculated with respect to $N_{2\,(g)}$, and E_C is the electronic energy of a C atom calculated with respect to pristine graphene. For models that include a Ni adatom, the energy of Ni in its bulk state is used as reference. The calculated ΔE_{def} values are reported in Table S2.

II. Supplementary figures

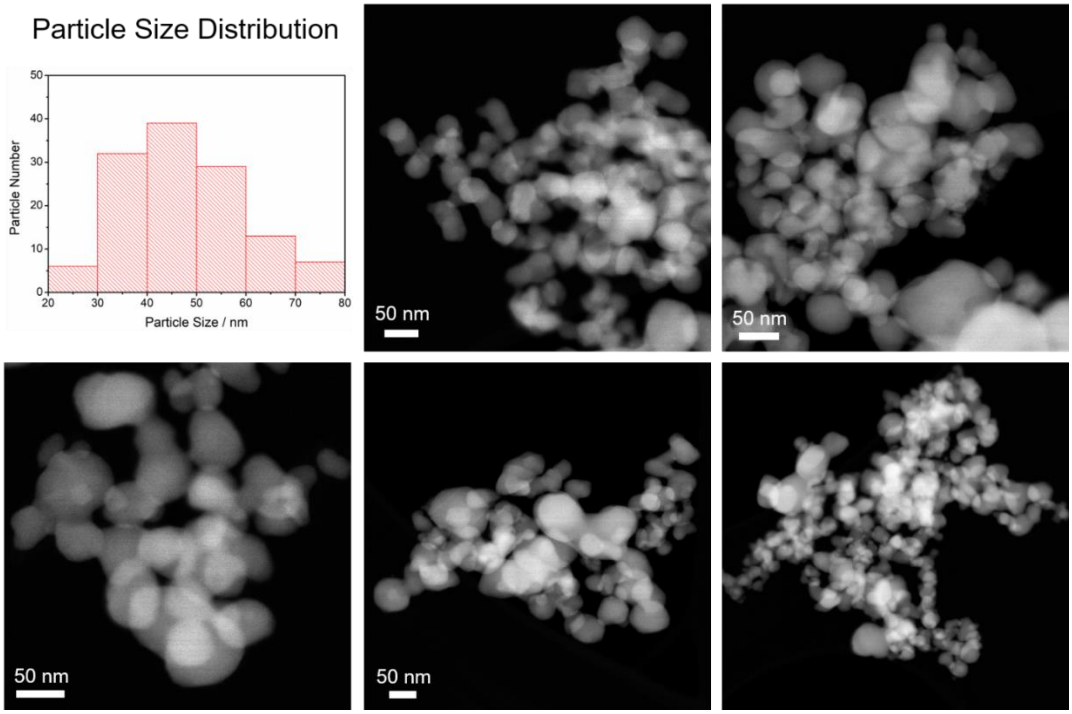

Figure S1. **Particle size distribution of Ni@CN$_x$.** Around 300 nanoparticles were analyzed from the above five STEM images.

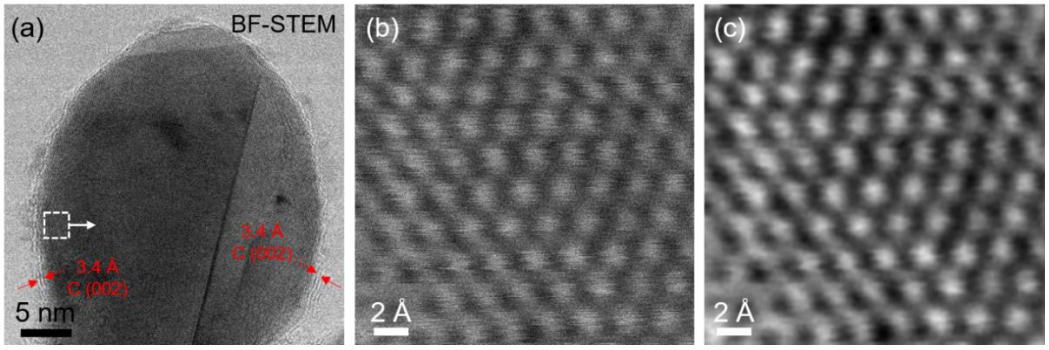

Figure S2. (a) BF-STEM images of one Ni@CNx nanoparticle, corresponding to the image in Figure 1c. (b) Raw atomic-scale STEM image was enlarged from the dashed white box in (a). (c) The raw STEM image was processed using Richard-Lucy deconvolution (3 iterations) to partially remove the scan noise during image acquisition. The deconvolution was processed in ImageJ software assuming an Airy disk (100 kV, αmax=28 mrad) convolved with a 0.8 Å Gaussian source.[13,14]

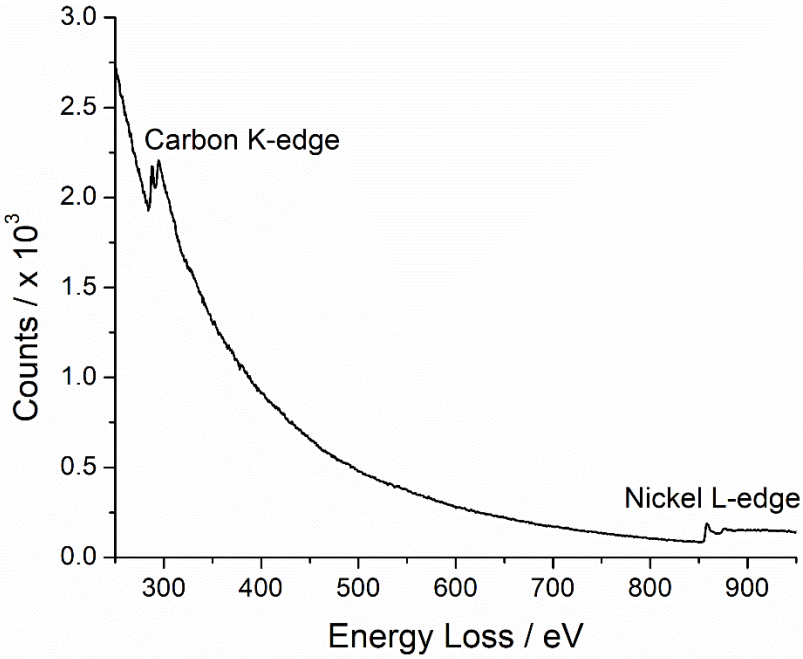

Figure S3. **EELS spectrum of Ni@CNx with the pronounced C K-edge and Ni L-edge**. No noticeable N signal was detected at around 400 eV due to the relatively low content of N in the catalysts. Instead, the detection of the N signal will rely on XPS analysis.

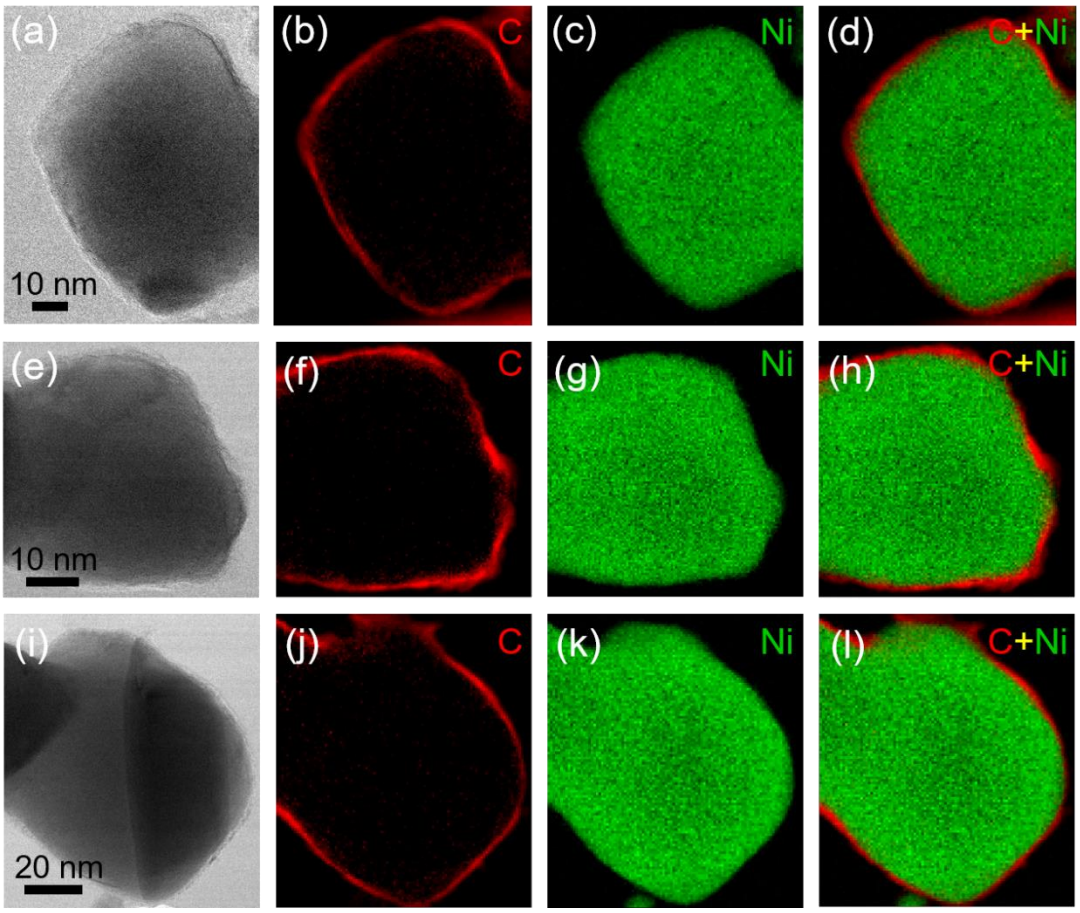

Figure S4. STEM images and EELS elemental maps of three Ni@CN_x nanoparticles with a carbon shell of 1-3 nm.

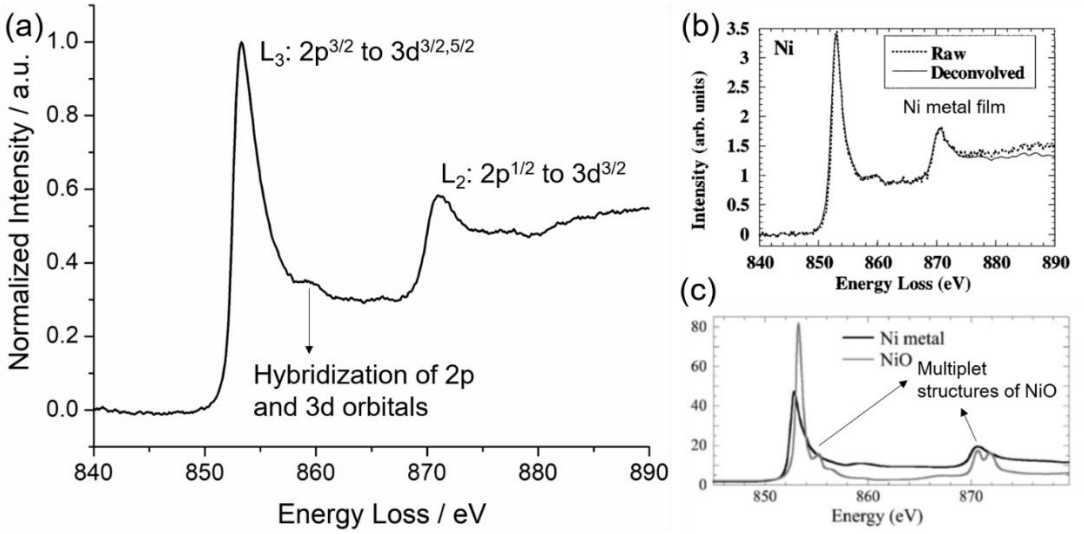

Figure S5. (a) ELNES (fine EELS) spectrum of Ni $L_{3,2}$ edges with a shoulder peak at around 860 eV. (b) EELS spectra of a 15nm-thick Ni metal film with the same shoulder peak at around 860 eV. Adapted from Ref.[15] with permission. Copyright@APS. (c) Standard synchrotron-based XAS spectra of Ni metal and NiO. Adapted from Ref.[16,17] with permission. Copyright@APS. This comparison suggests the formation of metallic Nickel. No evidence of Ni-N bonds was found.

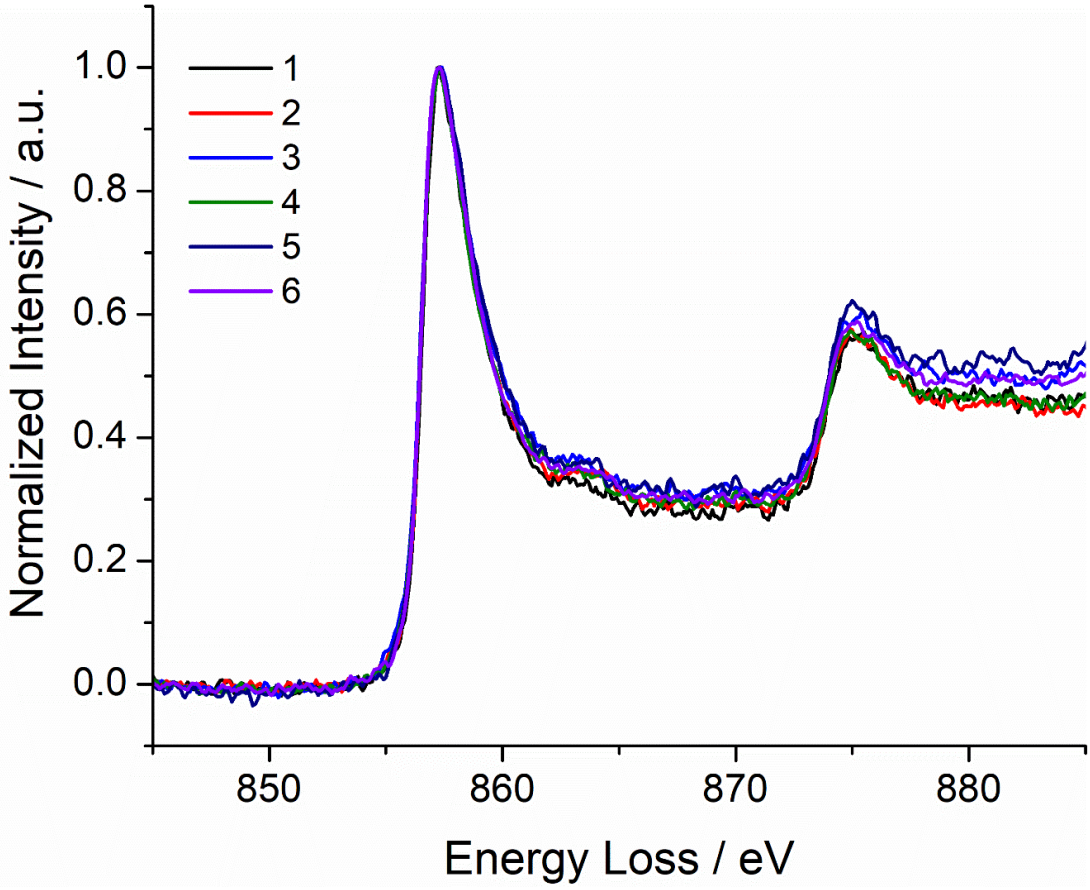

Figure S6. The ELNES spectra of Ni L edges were examined for reproducibility at six random selected regions. The average ELNES of six regions served as the final spectrum in Figure 1j.

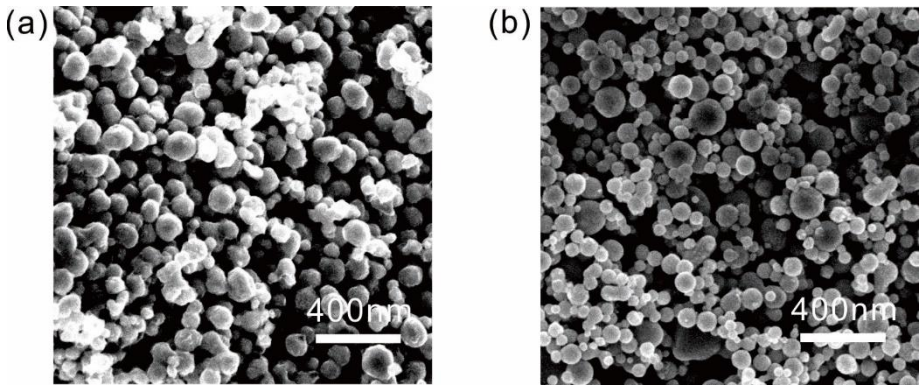

Figure S7. The SEM images of Ni@CN_x (a) and Ni NPs (b)

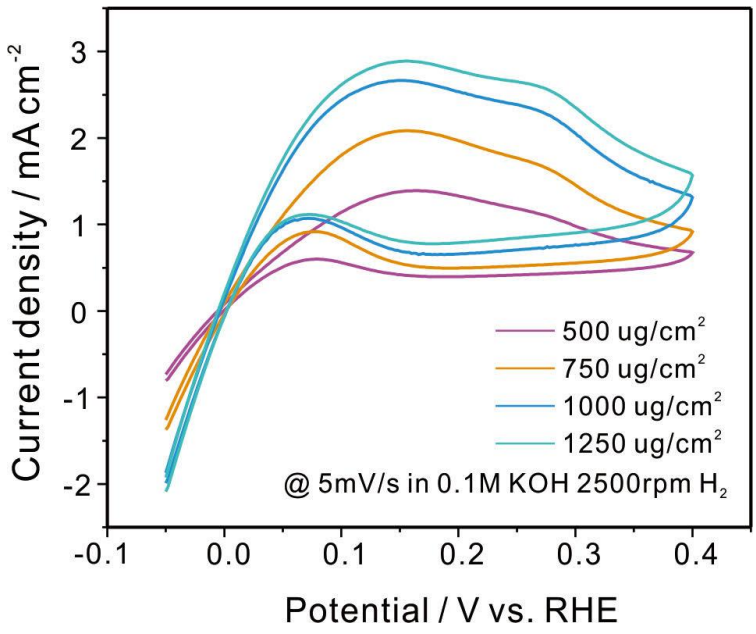

Figure S8. CV profiles of Ni@CN_x with various loadings.

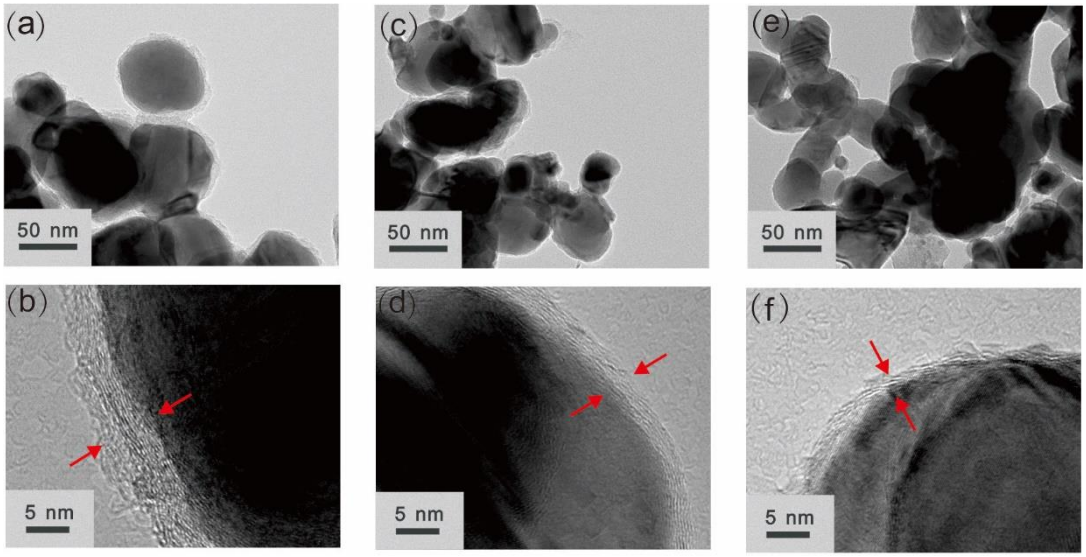

Figure S9. The TEM and HRTEM images of different samples. (a) and (b) refers to Ni@CN_x-1; (c) and (d) refers to Ni@CN_x-2; (e) and (f) refers to Ni@CN_x-3. The thickness of the CN shells varied from 5nm to 3nm and 1nm, respectively.

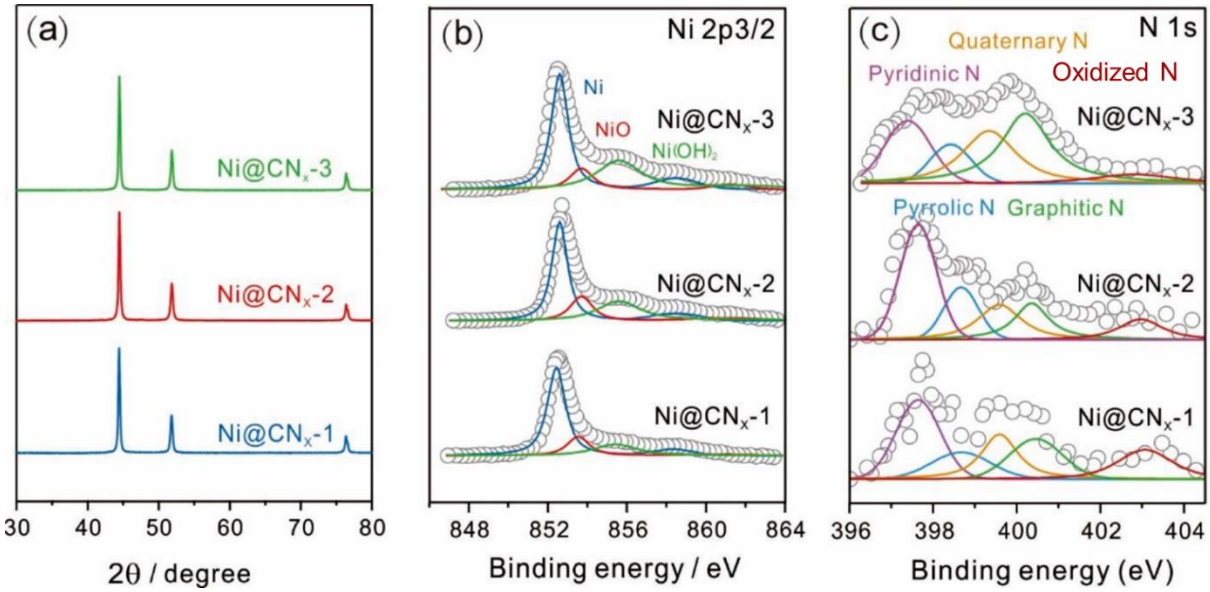

Figure S10. XRD patterns and XPS spectra of three different Ni@CN_x samples, (a) XRD data for Ni@CN_X catalysts, (b) XPS Ni2$p_{3/2}$ spectra for Ni@CN_x. (c) XPS N1s for Ni@CN_x.

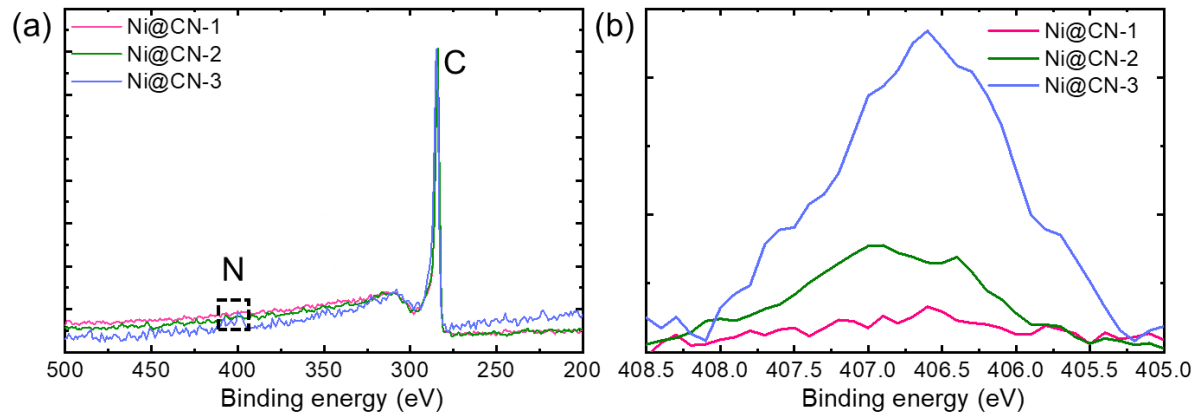

Figure S11. (a) Full XPS spectra and (b) high-resolution XPS spectra of N peaks of Ni@CN-1, 2 and 3 after normalization to the C peaks. The mass ratio of urea to nickel acetate ($Ni(Ac)_2$) was controlled to be 1:30, 1:15 and 1:10, labeled as $Ni@CN_x$-1, $Ni@CN_x$-2 and $Ni@CN_x$-3, which have N/C ratios of 1.65, 2.29 and 6.84%, respectively.

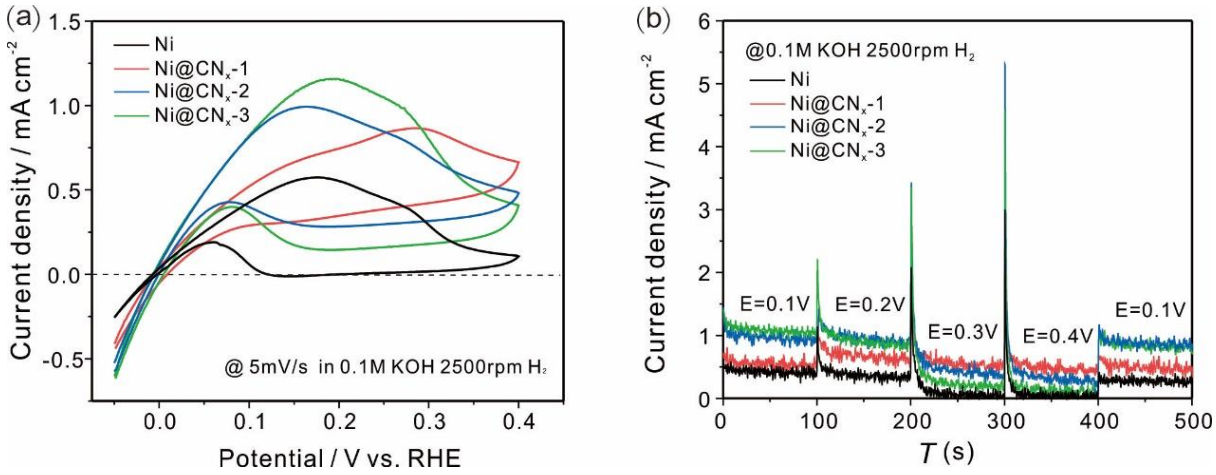

Figure S12. CV and CVP profiles of different samples, (a) CV profiles of Ni NPs and $Ni@CN_x$ with different shell thickness. (b) Constant-potential polarization (CVP) profiles of catalysts.

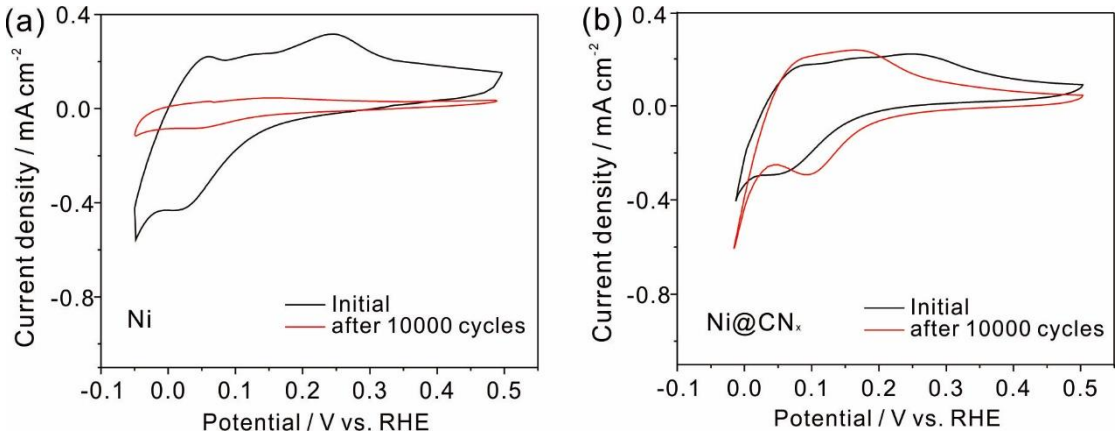

Figure S13. CV profiles of Ni particles and Ni@CN_x before and after ADT tests at a scan rate of 5 mV/s in Ar-sat. 0.1 M KOH.

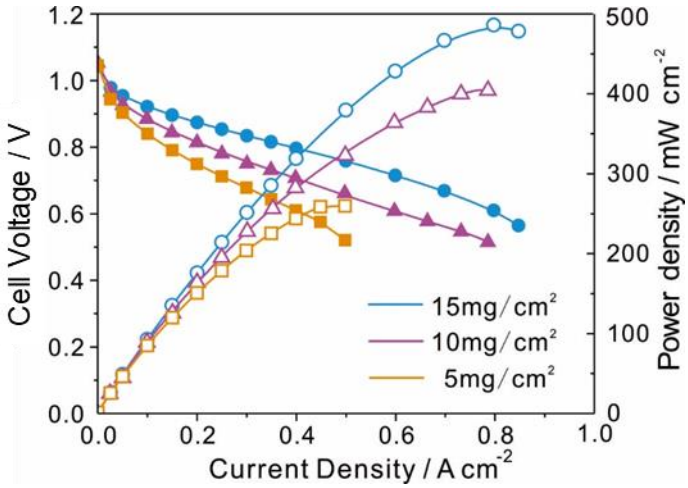

Figure S14. The APEFCs performance with different Ni@CN_x catalysts loadings. Pt/C cathode had a Pt loading of 0.4 mg/cm^2. Fuel cell operation conditions: cell temperature of 80 ºC, backpressure of 0.2 MPa on both sides of the cell. Fully humidified H_2 and O_2 were fed at a flow rate 500 mL/min.

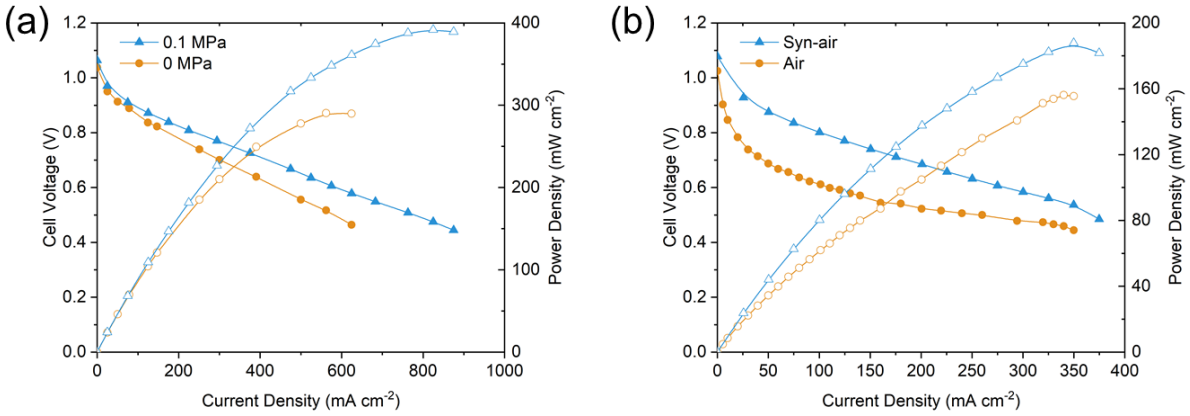

Figure S15. (a) APEFCs performance with a Ni@CN_x anode (15 mg_{Ni}/cm^2) and a 60 wt.% Pt/C cathode (0.4 mg_{Pt}/cm^2) at different backpressures. Fuel cell operation conditions: cell temperature of 80 ºC, fully humidified H_2 and O_2 were fed at a flow rate 500 mL/min. (b) APEFCs performance with a Ni@CN_x anode (15 mg_{Ni}/cm^2) and a 20 wt.% Pt/C cathode (0.2 mg_{Pt}/cm^2) with synthetic air (syn-air) and regular air containing 400 ppm CO_2. Fuel cell operation conditions: cell temperature of 80 ºC, backpressure of 0.2 MPa on both sides of the cell. Fully humidified H_2 and syn-air or regular air were fed at a flow rate 500 mL/min.

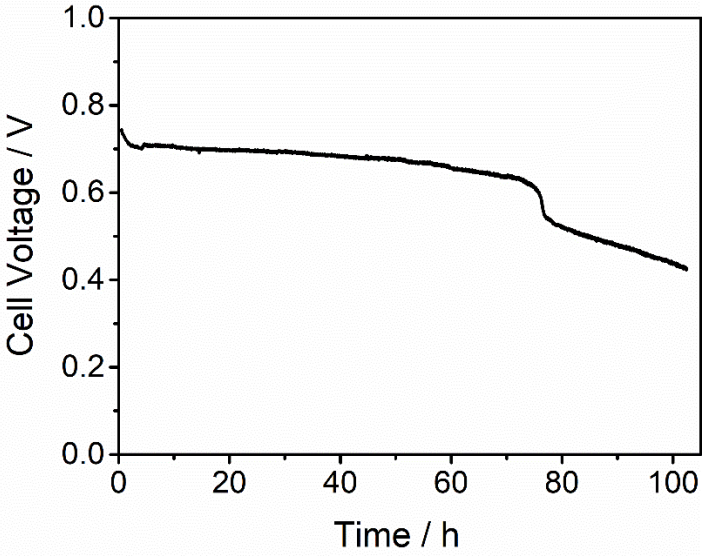

Figure S16 MEA durability of a Ni@CN_x anode (15 mg_{Ni}/cm^2) and a Pt/C cathode (0.4 mg/cm^2). Fuel cell operation conditions: Cell temperature of 80 ºC, H_2-O_2 (0.2/0.2 MPa, fully humidified) at a flow rate of 500 mL/min.

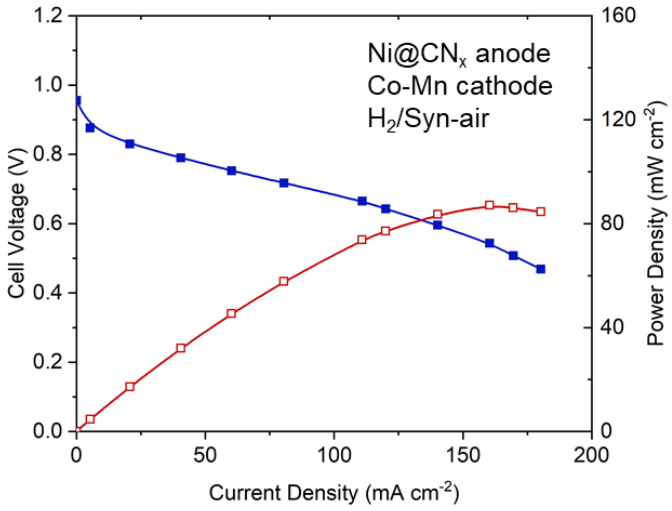

Figure S17 MEA performance with a Ni@CN_x anode (15 mg/cm^2), and an 80 wt.% $MnCo_2O_4$/C (1.5 mg_{oxide}/cm^2) cathode. Fuel cell operation conditions: Cell temperature of 80 ºC, H_2/Syn-air (0.2/0.2 MPa, 100%/100% RH) at a flow rate of 500 mL/min.

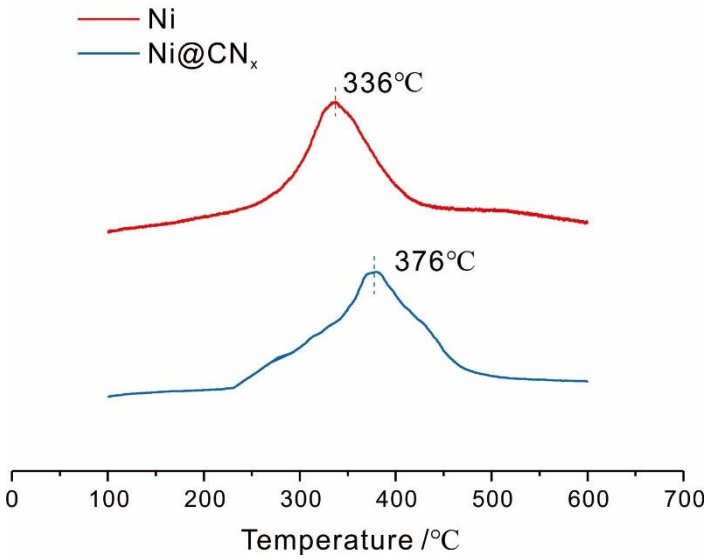

Figure S18. The TPO data of Ni particles and Ni@CN_x. The samples were initially maintained in Ar (50mL/min) at 100 ºC for 30 min and heated in 10% (v/v) O_2-He (50mL/min) from 100 ºC to 600 ºC with a ramping rate of 5 ºC/min.

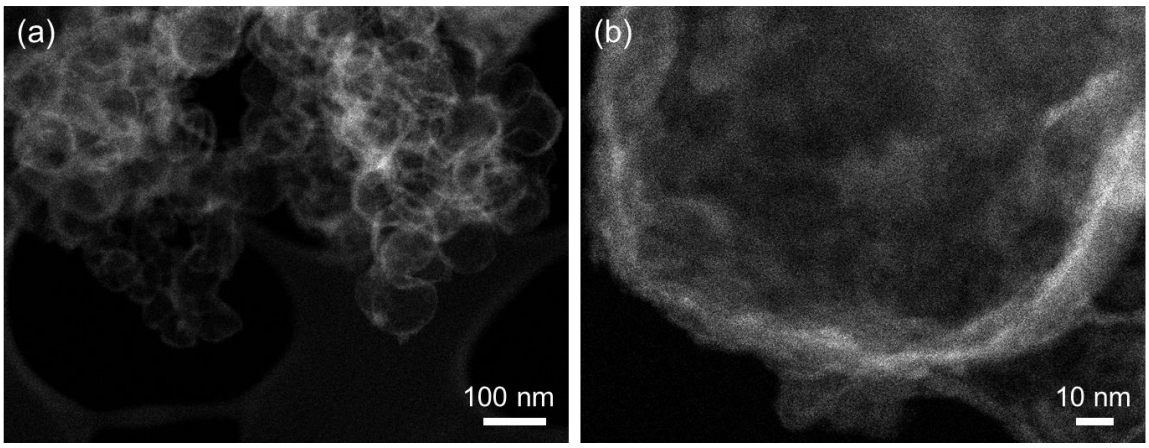

Figure S19. (a-b) STEM images of Ni@CN_x after acid washing.

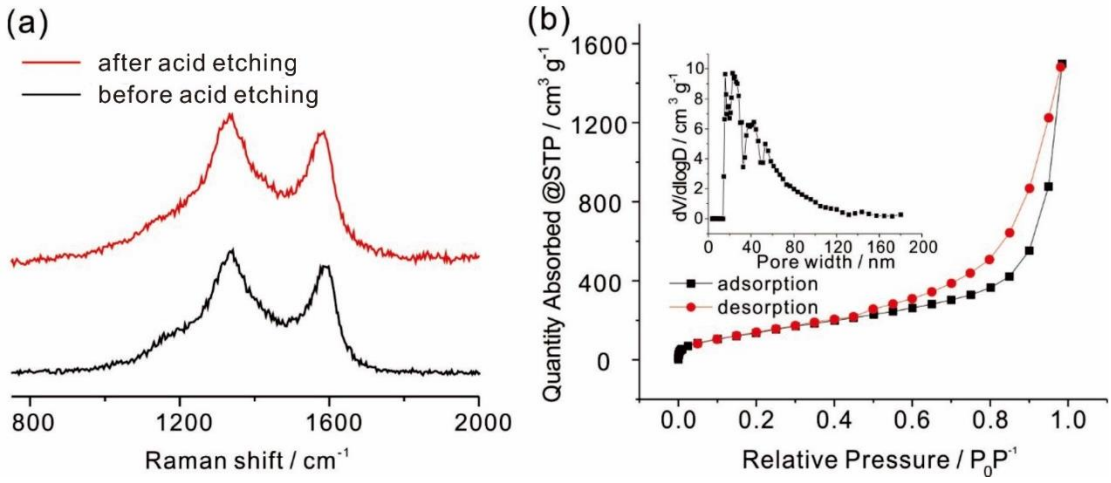

Figure S20. (a) Raman spectra of Ni@CN_x before and after acid etching and (b) BET analysis of CN_x shells. The inset is the pore size distribution.

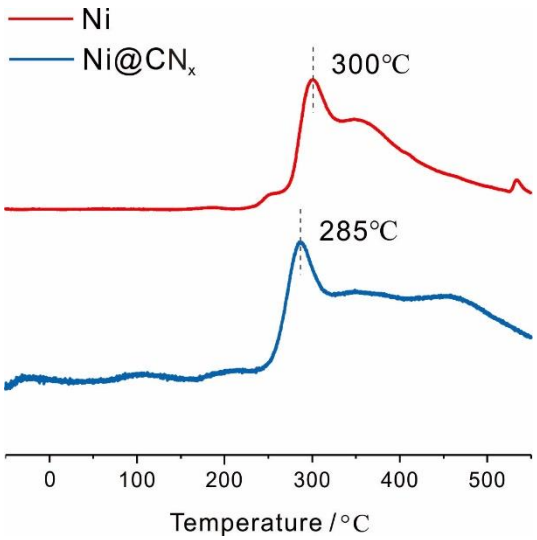

Figure S21. The H-TPD data of Ni@CN_x and Ni NPs. The samples were initially exposed to 10% (v/v) H_2-Ar atmosphere (50mL/min) at 150 ºC for 60 min, then changed to Ar (50mL/min) to purge the chemisorbed H on the samples at 400 ºC for 30 min. After cooling down to -50 ºC, the samples were exposed to 10% (v/v) H_2-Ar atmosphere (50mL/min) for 15 min and heated in Ar (50mL/min) to 550 ºC at a ramping rate of 5 ºC/min.[18]

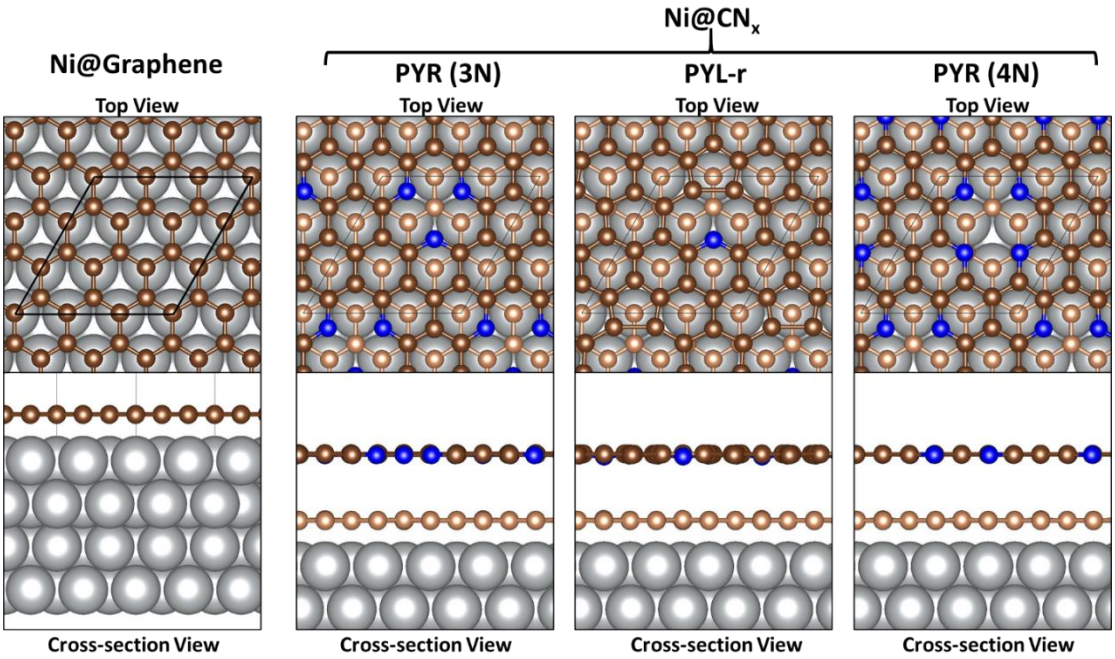

Figure S22. Optimized geometry of Ni@Graphene and Ni@CN_x models. Top and cross-sectioned views are shown in the upper and bottom panel, respectively. Ni, C, and N atoms are represented by silver, brown, and blue spheres, respectively. Graphene atoms in direct contact with Ni atoms in Ni@CN_x models are colored in light brown, while graphene in the second layer is colored in dark brown.

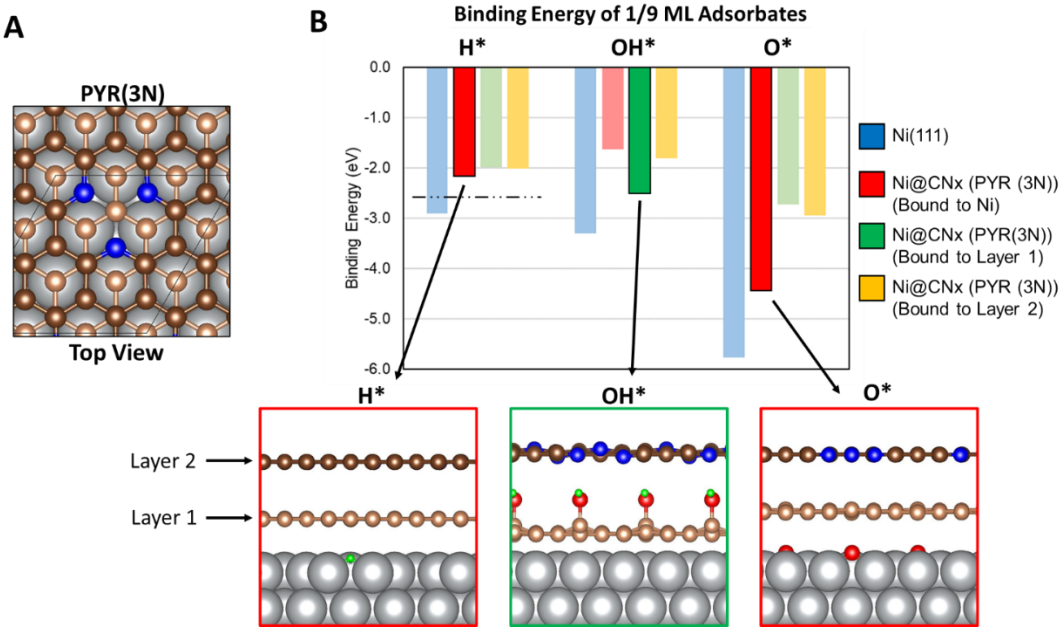

Figure S23. Binding energy of reaction intermediates H* and OH* and catalyst poison O* on pristine Ni(111) and Ni@CN_x including a PYR (3N) defect. (A) Top view of the PYR (3N) defect; (B) Adsorbate binding energies (in eV). Blue, red, green, and yellow bars indicate the binding energy of adsorbates on a pristine Ni(111) surface, on Ni in graphene-coated Ni(111), on top of the graphene layer closest to Ni(111) (layer 1), and on the defective graphene layer (1ayer 2), respectively. The dashed line corresponds to the optimal binding of H*. Bolded bars denote the most stable H*, OH*, and O* states. The cross-sectioned view of the most stable H*, OH*, and O* energy-optimized structures are reported below the chart. Ni, C, O, and H atoms are represented by silver, brown, red, and green spheres, respectively. Graphene atoms in direct contact with Ni atoms in Ni@CN_x models are colored in light brown (layer 1), while graphene in the second layer is colored in dark brown (layer 2).

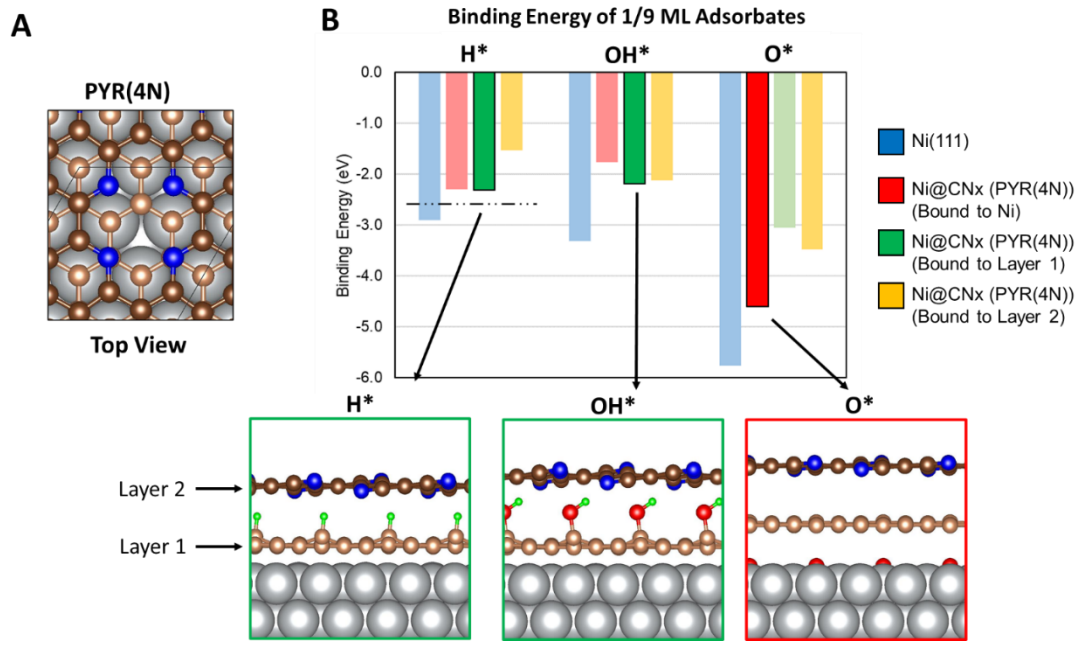

Figure S24. Binding energy of key reaction intermediates H* and OH* and catalyst poison O* on pristine Ni(111) and Ni@CN_x including a PYR (4N) defect. (A) Top view of the PYR (4N) defect; (B) Adsorbate binding energies (in eV). Blue, red, green, and yellow bars indicate the binding energy of adsorbates on a pristine Ni(111) surface, on Ni in graphene-coated Ni(111), on top of the graphene layer closest to Ni(111) (layer 1), and on the defective graphene layer (1ayer 2), respectively. The dashed line corresponds to the optimal binding of H*. Bolded bars denote the most stable H*, O*, and O* states. The cross-sectioned view of the most stable H*, O*, and OH* energy-optimized geometries are reported below the chart. Ni, C, O, and H atoms are represented by silver, brown, red, and green spheres, respectively. Graphene atoms in direct contact with Ni atoms in Ni@CN_x models are colored in light brown (layer 1), while graphene in the second layer is colored in dark brown (layer 2).

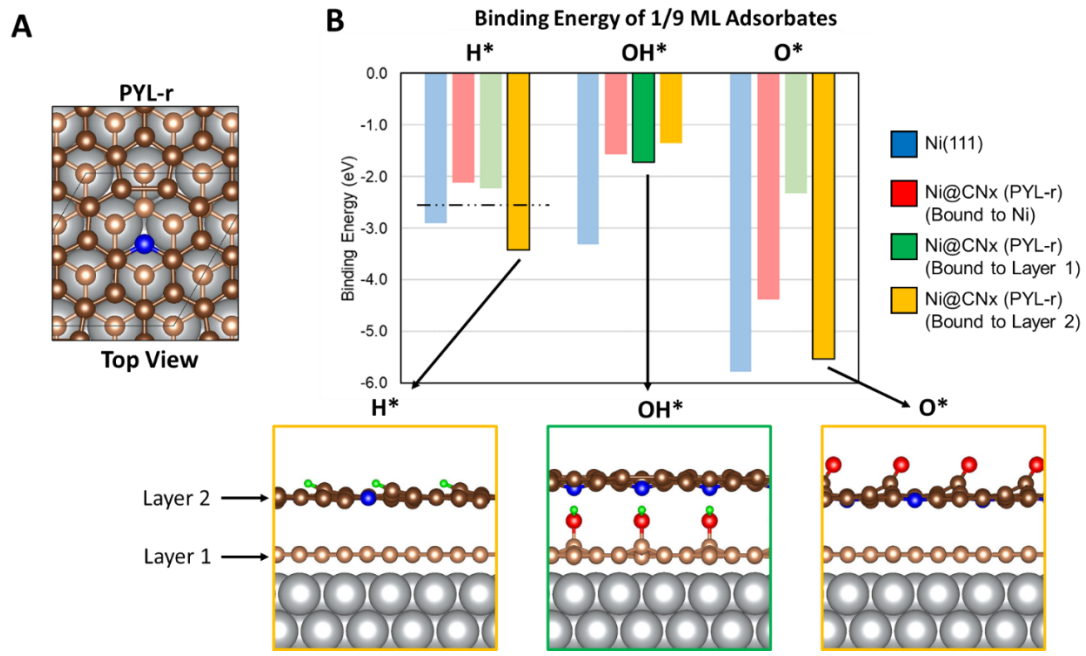

Figure S25. Binding energy of key reaction intermediates H* and OH* and catalyst poison O* on pristine Ni(111) and Ni@CN_x including a PYL-r defect. (A) Top view of the PYL-r (3N) defect; (B) Adsorbate binding energies (in eV). Blue, red, green, and yellow bars indicate the binding energy of adsorbates on a pristine Ni(111) surface, on Ni on graphene-coated Ni(111), on top of the graphene layer closest to Ni(111) (layer 1), and on the defective graphene layer (1ayer 2), respectively. The dashed line corresponds to the optimal binding of H*. Bolded bars indicate the most stable H*, OH*, and O* states. The side view of the most stable H*, OH*, and O* optimized geometries are reported below the chart. Ni, C, O, and H atoms are represented by silver, brown, red, and green spheres, respectively. Graphene atoms in direct contact with Ni atoms in Ni@CN_x models are colored in light brown (layer 1), while graphene in the second layer is colored in dark brown (layer 2).

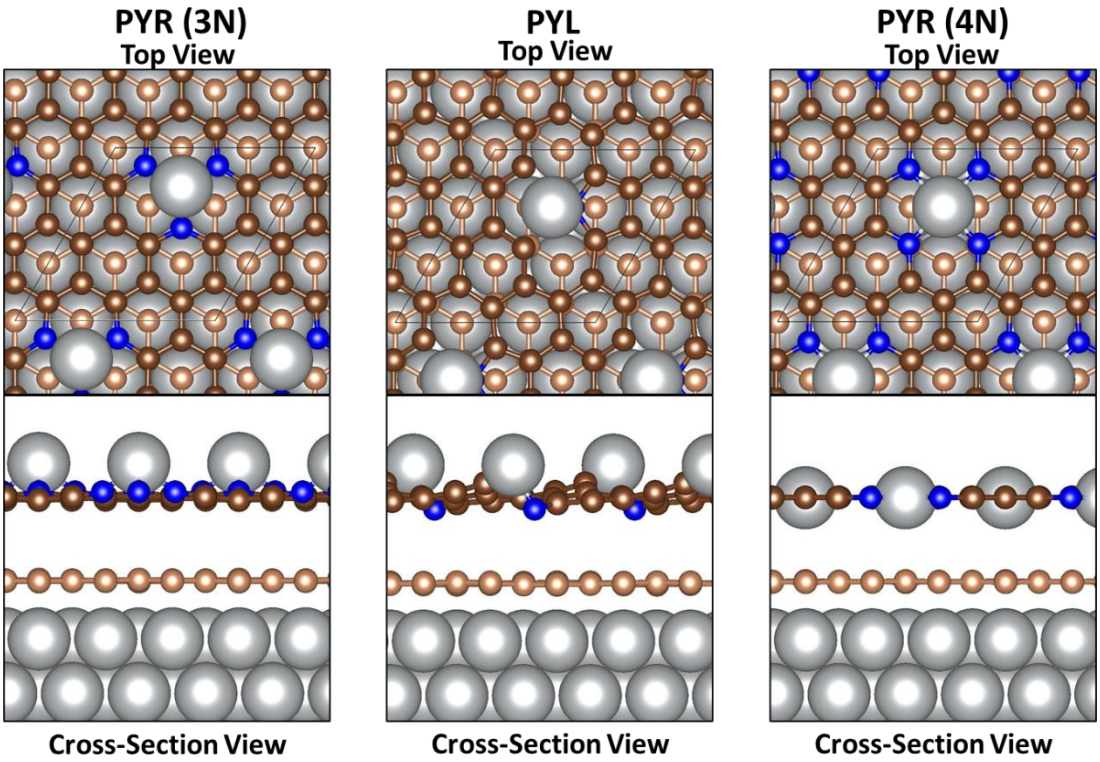

Figure S26. Energy-optimized geometry of Ni adatoms supported on Ni@CN_x models, including PYR (3N), PYL, and PYR (4N) defects. Top and cross-section views are reported in the upper and bottom panel, respectively. Ni, C, and N atoms are represented by silver, brown, and blue spheres, respectively. Graphene atoms in direct contact with Ni atoms in Ni@CN_x models are colored in light brown, while graphene in the second layer is colored in dark brown.

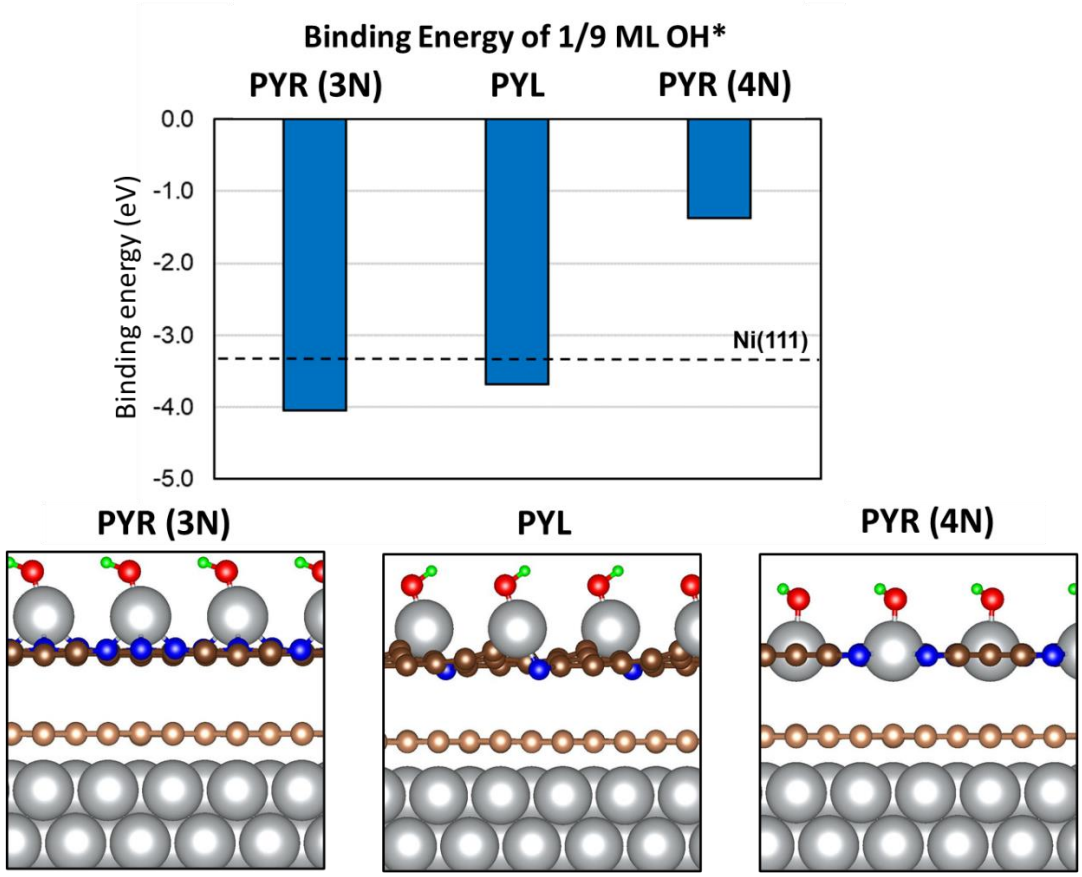

Figure S27. Binding energy of OH on Ni@CN_x models in the presence of Ni adatoms. Dashed horizontal line in bar chart indicates the binding energy of OH* on Ni(111) (-3.31 eV). The cross-sectioned view of the most stable OH* energy-optimized geometry on each Ni@CN_x defective model is reported below the bar chart. Ni, C, N, O, and H atoms are represented by silver, brown, blue, red, and green spheres, respectively. Graphene atoms in direct contact with Ni atoms in Ni@CN_x models are colored in light brown, while graphene in the second layer is colored in dark brown.

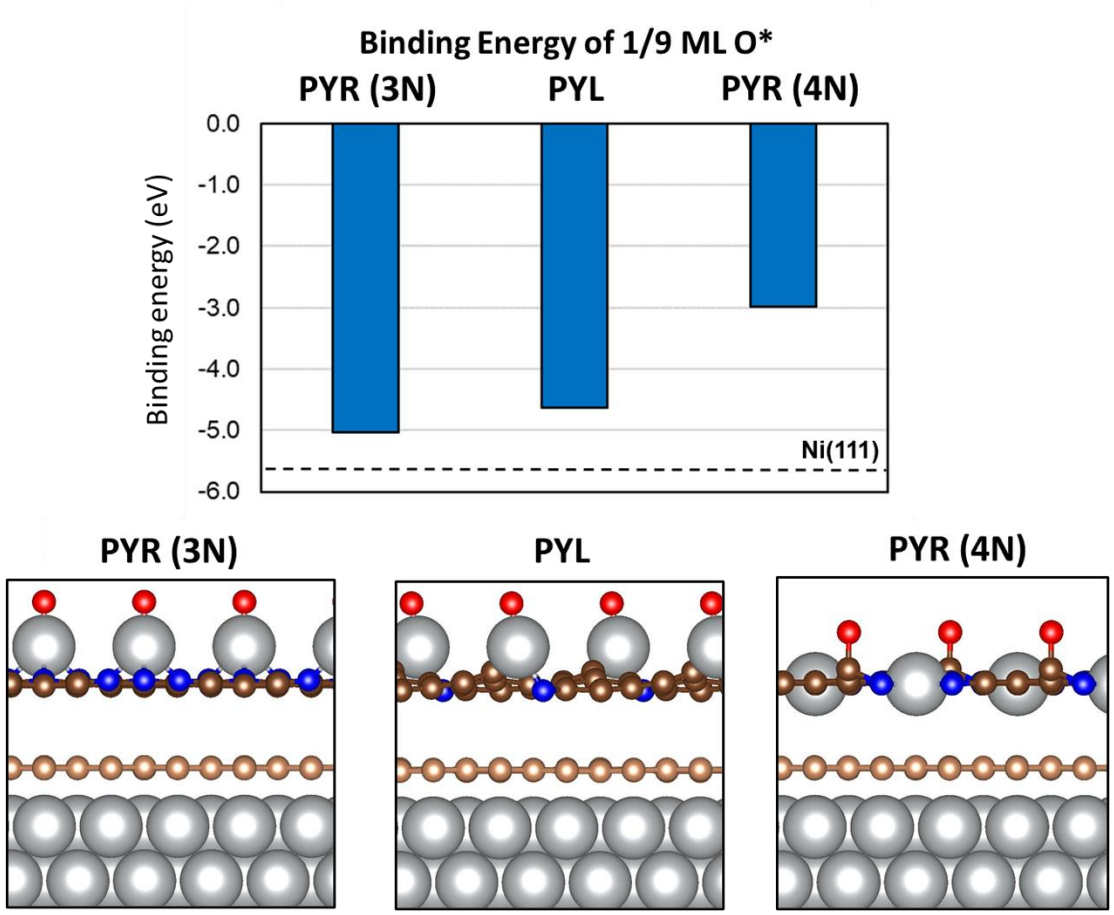

Figure S28. Binding energy of O on Ni@CN_x models in the presence of Ni adatoms. Dashed line on bar chart indicates the binding energy of O* on Ni(111) (-5.77 eV). The cross-sectioned view of the most stable O* energy-optimized geometry on each Ni@CN_x defective model is reported below the chart. Ni, C, N, and O atoms are represented by silver, brown, blue, and red spheres, respectively. Graphene atoms in direct contact with Ni atoms in Ni@CN_x models are colored in light brown, while graphene in the second layer is colored in dark brown.

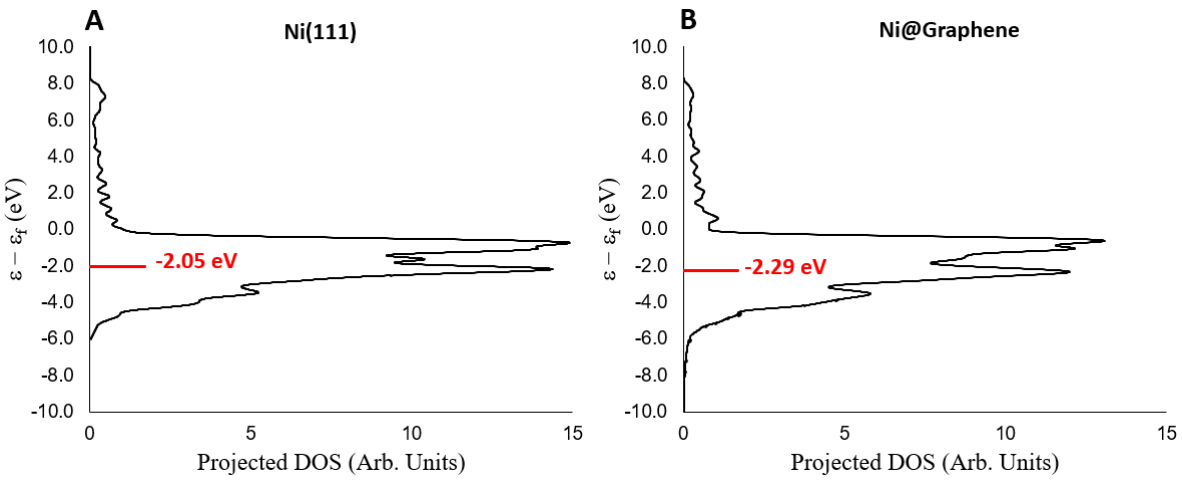

Figure S29. Projected density of states (DOS). Density of d-orbital states projected on surface Ni atoms in (A) Ni(111) and (B) Ni@Graphene. The value of the d-band center is indicated by a red line.

Table S1. The cell performance of Ni@CN_x and comparison to other literature reported non-precious metal anode catalysts in literatures.

Anode catalysts	Cathode catalysts	Temperature (°C)	Peak power density (mW/cm^2)	Ref.
Ni-CrO_x	Pt	60	50	S18
Ni-WO_x	CoPPY	60	40	S19
Ni-MoO_x	Pd	70	120	S20
Ni-Cu	Pd	80	350	S21
Ni@CN_x	Pt	80	480	This work
Ni@CN_x	CoMn	80	210	This work

Table S2. Calculated defect formation energy (ΔE_{Def}) and Total Magnetic moment per Ni atom on Ni@CN_x models.

Model	**ΔE_{Def} (eV)**	**Magnetic Moment/Ni (μ_B)**
PYR (3N) (1L)	1.96	0.62
PYR (4N) (1L)	2.44	0.61
PYL (1L)	5.07	0.59
PYR (3N) (2L)	3.30	0.62
PYR (4N) (2L)	3.75	0.61
PYL-r (2L)	5.80	0.62
Ni adatom/PYR(3N) (2L)	4.37	0.63
Ni adatom/PYR(4N) (2L)	1.36	0.60
Ni adatom/PYL (2L)	9.06	0.63

Table S3: Binding Energy of Adsorbates (in eV) on Ni(111) and Ni@Graphene Surfaces

Adsorbate	Ni(111)	Ni(111)+Graphene (Bound to Surface)	Ni(111)+Graphene (Bound to Graphene)
H*	-2.90	-2.62	-2.33
OH*	-3.31	-2.14	-2.43
O*	-5.77	-4.97	-3.72

Table S4: Binding Energy of Adsorbates (in eV) on Ni(111) and Ni@CN_x Surfaces with PYR (3N) Defect.

Adsorbate	Ni(111)	Ni(111) + 2L Defective Graphene (Bound to Ni)	Ni(111) + 2L Defective Graphene (Bound to Graphene Layer 1)	Ni(111) + 2L Defective Graphene (Bound to Graphene Layer 2)
H*	-2.90	-2.17	-1.98	-2.01
OH*	-3.31	-1.63	-2.50	-1.80
O*	-5.77	-4.44	-2.73	-2.95

Table S5: Binding Energy of Adsorbates (in eV) on Ni(111) and Ni@CN_x Surfaces with PYR (4N) Defect

Adsorbate	Ni(111)	Ni(111) + 2L Defective Graphene (Bound to Ni)	Ni(111) + 2L Defective Graphene (Bound to Graphene Layer 1)	Ni(111) + 2L Defective Graphene (Bound to Graphene Layer 2)
H*	-2.90	-2.30	-2.32	-1.53
OH*	-3.31	-1.77	-2.19	-2.13
O*	-5.77	-4.60	-3.05	-3.47

Table S6: Binding Energy of Adsorbates (in eV) on Ni(111) and Ni@CN_x Surfaces with PYL-r Defect.

Adsorbate	Ni(111)	Ni(111) + 2L Defective Graphene (Bound to Ni)	Ni(111) + 2L Defective Graphene (Bound to Graphene Layer 1)	Ni(111) + 2L Defective Graphene (Bound to Graphene Layer 2)
H*	-2.90	-2.12	-2.23	-3.43
OH*	-3.31	-1.57	-1.71	-1.35
O*	-5.77	-4.38	-2.33	-5.53

Table S7: Binding Energy of Adsorbates (in eV) on Ni adatoms supported on Ni@CN_x models, including PYR (3N), PYL, and PYR (4N) defects

Adsorbate	Ni(111)	PYR (3N) + Ni Adatom	PYL + Ni Adatom	PYR (4N) + Ni Adatom
H*	-2.90	-2.72	-2.69	-0.92
OH*	-3.31	-4.05	-3.68	-1.37
O*	-5.77	-5.03	-4.64	-2.98

IV. References

1. Y. Yang, Y. Xiong, M. E. Holtz, X. Feng, R. Zeng, G. Chen, F. J. DiSalvo, D. A. Muller, H. D. Abruña, Octahedral Spinel Electrocatalysts for Alkaline Fuel Cells. *Proc. Natl. Acad. Sci*. **116**, 24425-24432 (2019).
2. H. Ren, Y. Wang, Y. Yang, X. Tang, Y. Peng, H. Peng, L. Xiao, J. Lu, H. D. Abruña, L. Zhuang, Fe/N/C nanotubes with atomic Fe sites: a highly active cathode catalyst for alkaline polymer electrolyte fuel cells. *ACS Catalysis* **7**, 6485-6492 (2017).
3. Kresse, G. & Furthmüller, J. Efficient iterative schemes for Ab Initio total-energy calculations using a plane-wave basis set. Phys. Rev. B 54, 11169–11186 (1996).
4. Kresse, G. & Furthmüller, J. Efficiency of Ab-Initio total energy calculations for metals and semiconductors using a plane-wave basis set. Comput. Mater. Sci. 6, 15–50 (1996).
5. Perdew, J. P., Burke, K. & Ernzerhof, M. Generalized gradient approximation made simple. Phys. Rev. Lett. 77, 3865–3868 (1996).
6. Grimme, S. Semiempirical GGA-type density functional constructed with a long-range dispersion correction. J. Comput. Chem. 27, 1787–1799 (2006).
7. Muñoz-Galán, H., Viñes, F., Gebhardt, J., Görling, A. & Illas, F. The contact of graphene with Ni(111) surface: description by modern dispersive forces approaches. Theor. Chem. Acc. 135, 1–9 (2016).

8. Zhang, W. B., Chen, C. & Tang, P. Y. First-principles study for stability and binding mechanism of graphene/Ni(111) interface: role of VdW interaction. J. Chem. Phys. 141, 044708 (2014).
9. Cahangirov, S., Ciraci, S. & Özçelik, V. O. Superlubricity through graphene multilayers between Ni(111) surfaces. Phys. Rev. B - Condens. Matter Mater. Phys. 87, 205428 (2013).
10. Lide, D. R. CRC Handbook of Chemistry and Physics, 87th ed., CRC Press (2006).
11. Monkhorst, H. J. & Pack, J. D. Special points for brillouin-zone integrations. Phys. Rev. B 13, 5188–5192 (1976).
12. Robertson, A. W., Montanari, B., He, K., Allen, C. S., Wu, Y. A., Harrison, N. M., Kirkland, A. I. & Warner, J. H. Structural reconstruction of the graphene monovacancy. ACS Nano 7 4495–4502 (2013).
13. Kirkland, E. *Advanced Computing in Electrons Microscopy*. Springer: New York (2010).
14. Wang, D., Xin, H., Hovden, R., Wang, H., Yu, Y., Muller, D. A., DiSalvo, F. & Abruña, H. D. Structurally ordered intermetallic platinum-cobalt core-shell nanoparticles with enhanced activity and stability as oxygen reduction electrocatalysts. *Nat. Mater*. **12**, 81-87 (2013).
15. Muller, D. A., Singh, D. J. & Silcox, J. Connections between the electron-energy-loss spectra, the local electronic structure, and the physical properties of a material: a study of nickel aluminum alloys. *Phys. Rev. B.* **57**, 8181 (1998).
16. Regan, T., Ohldag, H., Stamm, C., Nolting, F., Luning, J., Stohr, J. & White, R. L. Chemical effects at metal/oxide interfaces studied by X-ray-absorption spectroscopy. *Phys. Rev. B.* **64**, 214422 (2001).
17. Nesbitt, H. W., Legrand, D. & Bancroft, G. M. Interpretation of Ni2p XPS spectra of Ni conductors and Ni insulators. *Phys. Chem. Minerals.* **27**, 357-366 (2000).
18. Lu, S., Pan, J., Huang, A., Zhuang, L. & Lu, J. Alkaline polymer electrolyte fuel cells completely free from noble metal catalysts. *Proc. Natl. Acad. Sci. U.S.A.* **105**, 20611-20614 (2008).
19. Hu, Q., Li, G., Pan, J., Tan, L., Lu, J. & Zhuang, L. Alkaline polymer electrolyte fuel cell with Ni-based anode and Co-based cathode free from noble metal catalysts. *Int. J. Hydrogen Energ*. **38**, 16264-16268 (2013).
20. Kabir, S., Lemire, K., Artyushkova, K., Roy, A., Odgaard, M., Schlueter, D., Oshchepkov, A., Bonnefont, A., Savinova, E., Sabarirajan, D. C., Mandal, P., Crumlin, E. J., Zenyuk, I. V., Atanassov, P. & Serov, A. Platinum group metal-free NiMo hydrogen oxidation catalysts: high performance and durability in alkaline exchange membrane fuel cells. *J. Mater. Chem. A* **5**, 24433-24443 (2017).
21. Roy, A., Talarposhti, M. R., Normile, S. J., Zenyuk, I. V., Andrade, V. D., Artyushkova, K., Serov, A. & Atanassov, P. Nickel-copper supported on carbon black hydrogen oxidation catalyst integrated into anion-exchange membrane fuel cell. *Sustain. Energ. Fuels* **2**, 2268-2275 (2018).
22. Nørskov, J. K., Bligaard, T., Logadottir, A., Kitchin, J. R., Chen, J. G., Pandelov, S. & Stimming, U. Trends in the exchange current for hydrogen evolution. J. Electrochem. Soc. 152, J23 (2005).